

Tidally heated convection: Constraints on Europa's ice shell thickness

Gabriel Tobie, Gaël Choblet, and Christophe Sotin

Laboratoire Planétologie et Géodynamique, Université de Nantes, Nantes, France

Received 31 March 2003; revised 4 September 2003; accepted 12 September 2003; published 25 November 2003.

[1] The thickness of Europa's ice shell is constrained with numerical experiments of thermal convection, including heterogeneous tidal heating. Thermal convection occurs in the stagnant lid regime with most of the tidal heating located in the bottom half of the layer. The addition of tidal heating mainly results in the increase of the temperature of the well-mixed interior and in the decrease of the heat flux at the base of the ice layer. In many simulations, the ice in hot plumes is heated up to its melting point. This induces episodic upwellings (0.5 Ma) of partially molten ice up to the base of the conductive lid, with possible implications for the formation of lenticulae and chaos regions. The thickness of the convective ice shell in equilibrium with the heat flow from the silicate core is estimated to be about 20–25 km. Tidal dissipation and surface temperature variations create lateral variations of the ice shell thickness of about 5 km, with maxima near the equator at the Jovian and anti-Jovian points and minima at midlatitudes. Surface heat flux is about $35\text{--}40 \text{ mW.m}^{-2}$; it is almost constant all over Europa's surface, even though the tidal dissipation rate is four times larger at the poles than at the equator.

INDEX TERMS: 5430 Planetology: Solid Surface Planets: Interiors (8147); 5418 Planetology: Solid Surface Planets: Heat flow; 5770 Planetology: Fluid Planets: Tidal forces; 6020 Planetology: Comets and Small Bodies: Ice; 6218 Planetology: Solar System Objects: Jovian satellites; *KEYWORDS:* Europa, ice, tidal dissipation, thermal convection, equilibrium thickness

Citation: Tobie, G., G. Choblet, and C. Sotin, Tidally heated convection: Constraints on Europa's ice shell thickness, *J. Geophys. Res.*, 108(E11), 5124, doi:10.1029/2003JE002099, 2003.

1. Introduction

[2] During more than five years of observations of the Jovian system, the Galileo mission has returned a large amount of outstanding data. Two major discoveries are the complex tectonic of Europa's surface [Pappalardo *et al.*, 1999] and the magnetic signal from Europa's interior [Khurana *et al.*, 1998]. These constitute new strong indications of the presence of a subsurface ocean within Europa. Such an ocean is surprising since the satellite was expected to be frozen due to its very cold surface temperature ($\simeq 100 \text{ K}$). The Galileo measurements of Europa's external gravitational field have indicated that its internal structure consists of an outer H_2O shell of 100–200 km thickness overlying a silicate mantle and a metallic core [Anderson *et al.*, 1998; Sohl *et al.*, 2002]. Figure 1 shows one of the possible internal structures for Europa. The ratio of ice versus liquid water in the outer shell is unknown. The actual thickness of the ice shell is uncertain. Constraints on the ice thickness come from the interpretation of some features on Europa's surface that are relatively ambiguous. For instance, chaotic terrains are interpreted to be the result of the breakup of brittle surface materials over warm ductile ice [Pappalardo *et al.*, 1998] or to be an evidence for a near-surface ocean on Europa [Carr *et al.*, 1998; Greenberg *et*

al., 1999]. We believe that a more plausible explanation could be the presence of localized partial melt within the ice shell [Collins *et al.*, 2000]. Recently, Sotin *et al.* [2002] argued that in the range of ice viscosity inferred from laboratory experiments, tidal forces may heat up rising diapirs from the base of a thick ice shell and may produce melting temperatures in broad areas at shallow depths.

[3] For several years, tidal dissipation has been invoked to explain the possible presence of an ocean [Cassen *et al.*, 1979]. Tidal dissipation comes from the viscoelastic response of Europa to the 3.55-days tidal forcing. In the Laplace resonance, Io and Ganymede force the eccentricity of Europa. As it travels around Jupiter on an eccentric orbit, Europa is subjected to a periodical deformation. Due to the viscoelastic properties of its materials, viscous dissipation by shear friction occurs within each layer of Europa. The presence of a deep ocean would strongly modify its response to the tidal potential [Castillo *et al.*, 2000; Moore and Schubert, 2000] and the amount of tidally dissipated energy. Consequently, it would strongly affect the energy balance.

[4] Modeling thermal evolution and internal structure of Europa and other icy satellites also provides constraints on the outer shell thickness. Studies including tidal dissipation have been carried out since the Voyager mission. Previous models predicted that an ocean would persist beneath the ice shell if the effective dissipation factor Q of the ice is low (≤ 70) and if large tidal dissipation in the silicate core occurs

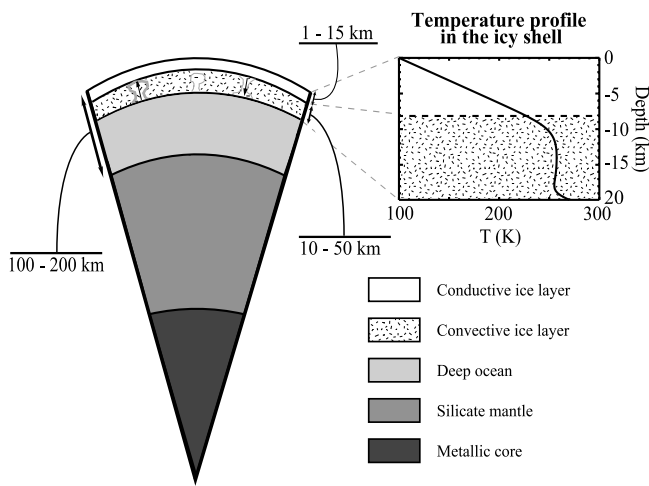


Figure 1. A possible 4-layer model for the radial structure of Europa and temperature profile in a 20-km floating ice shell. The physical parameters of each layer are presented in Table 1. The ice layer is composed of an outer conductive sublayer and an inner convective sublayer. The temperature profile of the 20-km ice shell has been computed with our 2D thermal convection model without taking into account the effect of tidal heating, for a bottom viscosity $\eta_{bot} = 10^{14}$ Pa.s and a viscosity ratio equal to 1.2×10^6 . The physical parameters of ice are presented in Table 2. Note that the thickness of the icy conductive lid is about 8 km.

[Squyres et al., 1983; Cassen et al., 1979]. Self-consistent calculations of tidal dissipation and conductive heat transfer through the ice shell lead to a relatively thin layer of ice (≤ 30 km) above a liquid ocean [Ojakangas and Stevenson, 1989]. These authors showed that tidal dissipation in the ice layer was sufficient to prevent the freezing of the ocean. These models assume that the ice layer (≤ 30 km) is stable against convective overturn. A previous study [Squyres et al., 1983] proposed that convection would initiate only for an ice shell thicker than 30 km, and, in that case, would transfer heat more efficiently and would accelerate the crystallization of a subsurface ocean.

[5] The issue of whether the ice shell is convecting or not is also debated. The major uncertainty is the rheology of the ice at both tidal strain rate and convective strain rate. Results for thermal convection of a fluid with strongly temperature dependent viscosity [e.g., Davaille and Jaupart, 1993; Moresi and Solomatov, 1995; Grasset and Parmentier, 1998; Dumoulin et al., 1999] provided a description for heat transfer in the asymptotic conductive lid regime. This has been applied to the rate of cooling of an icy satellite [Grasset and Sotin, 1996; McKinnon, 1999; Deschamps and Sotin, 2001; Ruiz, 2001; Hussmann et al., 2002; Spohn and Schubert, 2003]. For example, using such a scaling for stagnant lid convection [Solomatov, 1995] and recent laboratory results on ice rheology [Goldsby and Kohlstedt, 1997], McKinnon [1999] showed that ice shells as thin as 10 km would be unstable against convection at their base for melting-point viscosities of 10^{13} Pa.s, if the ice deforms by superplastic flow and if ice grain size is small (≤ 1 mm). Tidal heating depends on the viscosity and thus on the temperature of ice: when convection occurs, a large volume

of the ice may have a viscosity close to 10^{14} Pa.s and would dissipate large amounts of the deformation energy induced by the tidal flexion. Therefore the amount of tidal heating would be much larger than in the conductive ice shell case where tidal heating is concentrated in the 10% lower part of the layer [Ojakangas and Stevenson, 1989].

[6] A first attempt to assess the effect of tidal heating on convective heat transfer through the ice layer is presented by Hussmann et al. [2002]. With a steady-state parameterized model of convective and conductive heat transfer, the authors derive the thickness of a tidally heated ice shell in equilibrium with radiogenic heat flow from the silicate mantle, and they demonstrate that a convective layer does not transfer heat with enough efficiency to totally freeze the ocean and that relatively thin (~ 30 km) layer is thermally stable. Since no scaling law describing convective heat transfer for a layer, with a temperature-dependent viscosity, heated both from below and from within is yet available, we propose to investigate directly heat transfer through the ice shell with 2D-thermal convection numerical models. This is also motivated by the heterogeneous aspect of tidal heating and the probable occurrence of partial melting within Europa's ice shell [Wang and Stevenson, 2000; Sotin et al., 2002; Tobie et al., 2002], which cannot be a priori investigated with existing scaling laws.

[7] We carried out 2D numerical experiments of thermal convection with an infinite Prandtl number. We consider a Newtonian fluid with a strongly temperature-dependent viscosity and a realistic, viscosity-dependent, tidal heating. Melt production and transport, its influence on viscosity and buoyancy are also modeled. From these experiments, we derive the thickness of the ice shell in equilibrium with the heat flux from the silicate core. In section 2, we describe the numerical model for convection, the physical and numerical parameters and the computation of tidal dissipation within Europa. Section 3 presents the results of our calculations and their sensitivity to input parameters. These results are discussed in section 4.

2. Model

2.1. Two-Dimensional Dimensionless Dynamical Equations

[8] The infinite Prandtl number formulation is adopted in the Boussinesq approximation so that the dimensionless partial differential equations solved in this model, the conservation of mass (equation (1)), the conservation of momentum (equation (2)), the conservation of energy (equation (3)), can be written as follows:

$$\vec{\nabla} \cdot \vec{V}' = 0 \quad (1)$$

$$\vec{\nabla} \cdot [\eta(\vec{\nabla} \vec{V}' + (\vec{\nabla} \vec{V}')^t)] - \vec{\nabla} P' = Ra_{bot} \cdot T' \cdot \vec{e}_z + \vec{f}_{melt} \quad (2)$$

$$\frac{\partial T'}{\partial t'} = \nabla^2 T' - \vec{V}' \cdot \vec{\nabla} T' + h_{tide} \quad (3)$$

Primes refer to dimensionless variables:

$$x = bx'; z = bz'; P = \frac{\eta \kappa}{b^2} P'; \vec{V} = \frac{\kappa}{b} \vec{V}'; (T - T_{surf}) = \Delta T \cdot T' \quad (4)$$

b is the ice layer thickness, κ is the thermal diffusivity, ΔT is the temperature variation across the layer: $\Delta T = T_{bot} - T_{surf}$. P , T , V are respectively the fluid pressure, the temperature and the velocity.

[9] Ra_{bot} is the Rayleigh number defined for the whole layer and with the viscosity η_{bot} at the base of the ice shell:

$$Ra_{bot} = \frac{\alpha \rho g \Delta T b^3}{\kappa \eta_{bot}}, \quad (5)$$

with α thermal expansion, ρ mass per unit volume and g gravitational acceleration. f_{melt} is the dimensionless negative buoyancy due to melt fraction in the ice matrix. h_{tide} is the dimensionless tidal heating rate:

$$h_{tide} = \frac{H_{tide} b^2}{k \Delta T} \quad (6)$$

with k thermal conductivity. H_{tide} is the volumetric tidal heating rate (see section 2.3), varying in space and time.

2.2. Ice Viscosity

2.2.1. Rheology of Ice Near the Melting Point

[10] Low stress conditions typical of tidal deformation ($\sigma_{tide} = 0.01\text{--}0.1$ MPa) and convection ($\sigma_{conv} = 10^{-4}\text{--}10^{-3}$ MPa, deduced from our 2D thermal convection model) cannot be reproduced by laboratory mechanical tests, so that an extrapolation of results from higher stresses is required. Rheological data for crystalline material are usually described with a power-law relationship:

$$\dot{\epsilon} = A \frac{\sigma^n}{d^p} \exp\left(-\frac{Q + PV}{RT}\right) \quad (7)$$

where $\dot{\epsilon}$ is the strain rate, A is a material parameter, σ is the differential stress (or the second invariant of the stress tensor), n is the stress exponent, d is the grain size, p is the grain size exponent, Q is the activation energy, P is the hydrostatic pressure, V is the activation volume for creep, R is the gas constant. At high stresses, the rheology of ice is governed by intracrystalline dislocation slip mainly on basal plane with a stress exponent $n \geq 3$ [Budd and Jacka, 1989; Durham et al., 1997]. At lower differential stresses ($\sigma < 0.1$ MPa), the creep of ice may be controlled by Grain Boundary Sliding [Goldsby and Kohlstedt, 2001], or by both Dislocation Slip and Grain Boundary Sliding [Durham et al., 2001], or by Dislocation Slip accommodated by Grain Boundary Migration [Duval and Montagnat, 2002]. Several creep experiments also indicate a stress exponent lower than 2 for $\sigma \leq 0.1$ MPa (see Goldsby and Kohlstedt [2001, Table 4] for a review). The difficulty is to know how relevant are the extrapolation from experimental data to lower stresses (<0.01 MPa), and how ice samples used in mechanical tests are characteristic of Europa's ice. Furthermore, numerous parameters may influence the creep of ice. At temperatures near the melting point ($T > 240$ K), normal grain growth and changes in the fabric significantly influence the creep mechanism. In addition, the cyclic straining experienced by ice on Europa over 3.55 days may significantly modify its creep behavior, for example by increasing its dislocation density [Cole, 2001]. Thus the rheological behavior of ice cannot be dissociated a priori from its strain history.

[11] However, since most of these aspects are strongly constrained by thermally activated processes, we will

assume that the effective viscosity of ice mainly depends on temperature. In addition, the creep data inferred from polar ice sheets [Montagnat and Duval, 2000] indicate that ice tends to behave like a Newtonian fluid ($n = 1$) at very low strain rates ($\dot{\epsilon} < 10^{-11}\text{s}^{-1}$) and that the viscosity of ice near the melting point would be around $10^{13}\text{--}10^{15}$ Pa.s.

2.2.2. Effect of Premelting and Partial Melting on Ice Viscosity

[12] At temperatures close to the melting point, the strain rate is generally larger than the one predicted by extrapolating the lower temperature results. This is caused by premelting at grain boundaries and/or triple grain junctions at temperatures below the freezing point [Dash et al., 1995]. Due to impurities located at grain boundaries and to the geometry of grain junctions, a liquid film can develop for temperatures near the melting temperature of pure water ice. This premelting produces an enhancement of strain rate and consequently reduces the viscosity of ice. At the melting point, the liquid fraction increases strongly. A large enhancement of the creep rate has been observed in temperate glaciers with melt fractions of less than 1% [Duval, 1977]. De La Chapelle et al. [1999] showed that the presence of melt makes the internal stress more uniform within the polycrystal and increases the activity of the basal glide for low stresses, characterized by a stress exponent lower than 2. A melt fraction of about 5% increases the differential strain rate of about one order of magnitude [De La Chapelle et al., 1999].

2.2.3. Viscosity Law

[13] In the following, we assume that the viscosity of ice is Newtonian and depends on the temperature T and on the melt fraction x_m . The ice is assumed to be pure so that premelting effects are neglected. Viscosity decreases only when the melting point of pure ice is reached. We assume that the viscosity associated with both tidal and convective deformation is the same and that the rheological behavior of ice at tidal strain rates is well-described by a Maxwell model (see next section).

[14] In order to take into account the melt and temperature dependences of viscosity η , the following relationship is used:

$$\eta(T, x_m) = \eta_m \times \exp\left(-\gamma_T \frac{T - T_m}{\Delta T}\right) \times \exp(-\gamma_m \times x_m) \quad (8)$$

where η_m is the viscosity at the melting temperature, T_m is the melting temperature, ΔT is the temperature variation across the layer, γ_T and γ_m are two coefficients.

[15] The exponential formulation of the temperature dependence, termed Frank-Kamenetskii approximation, is commonly used in thermal convection models [see, e.g., Christensen, 1984; Moresi and Solomatov, 1995; Grasset and Parmentier, 1998; Reese et al., 1999]. When the exponential coefficient γ_T is adequately chosen:

$$\gamma_T = \frac{Q \Delta T}{R T_m^2}, \quad (9)$$

the accuracy of this approximation is about 4–5% on the temperature of the well-mixed interior [Reese et al., 1999]. For $Q = 50\text{kJ.mol}^{-1}$, $\Delta T = 170\text{K}$ and $T_m = T_{bot} = 270\text{K}$, $\gamma_T = 14$.

[16] For the melt dependence, no experimental law is yet available. Coefficient γ_m is chosen such that 5% melt induces one order of magnitude decrease of the viscosity: $\gamma_m = 45$. As mentioned before, this value is constrained by mechanical tests [De La Chapelle et al., 1999].

[17] The viscosity at the melting point varies between 10^{13} and 10^{15} Pa.s and remains constant with depth. Changes of the melting temperature with depth are too small (less than 3K) to influence significantly the model results and we take a constant value: $T_m = T_{bot} = 270\text{K}$.

2.3. Tidal Heating

[18] From the elastic formulation of the free spheroidal oscillation of a compressible planet [Takeuchi and Saito, 1972] adapted to the viscoelastic response of Europa by using the correspondence principle [Biot, 1954; Segatz et al., 1988], we have calculated the tidal dissipation distribution within an isotropic 4-layered Europa. We assume that Europa's interior behaves like a Maxwell body. In this condition, the Fourier transform of the stress-strain relationship can be written as a Hooke-like law:

$$\tilde{\sigma}_{ij} = (K - \frac{2}{3}\mu^c)\tilde{\epsilon}_{ii}\delta_{ij} + 2\mu^c\tilde{\epsilon}_{ij} \quad (10)$$

with $\tilde{\sigma}_{ij}$ the Fourier transform of stress tensor, $\tilde{\epsilon}_{ij}$ the Fourier transform of strain tensor, K bulk modulus, and $\mu^c = \mu^R + i\mu^I$ complex shear modulus defined as [Zschau, 1978]:

$$\mu^R = \frac{\eta^2 w^2 \mu_E}{\mu_E^2 + \eta^2 w^2} \quad \text{and} \quad \mu^I = \frac{\eta w \mu_E^2}{\mu_E^2 + \eta^2 w^2} \quad (11)$$

with w orbital frequency, μ_E elastic shear modulus, and η Newtonian viscosity. Following Takeuchi and Saito [1972], the complex radial functions y_i^c are computed as functions of the viscoelastic parameters of Europa's interior. The considered internal structure is in agreement with the measured moment of inertia ($C/MR^2 \simeq 0.35$) [Anderson et al., 1998] and the mean density of Europa. Table 1 presents the physical parameters used for each layer of the satellite. We then calculate the nine components of the strain and stress tensors and derive the rate of tidal dissipation per unit volume H_{tide} .

[19] Figure 2 shows the radial distribution of tidal dissipation rate per unit volume corresponding to the interior model described above. To compute dissipation in the ice shell, we use the viscosity profile obtained from our 2D convection model without tidal heating. At Europa's orbital frequency ($\omega = 2.10^{-5}\text{s}^{-1}$) forcing, maximum dissipation occurs in the ice layer at a viscosity around 10^{14} Pa.s, i.e., near the melting point viscosity. The amplitude of tidal deformation and consequently the amount of tidal heating depend on both latitude and longitude. At the base of the ice layer where the viscosity is expected to be close to 10^{14} Pa.s, maxima ($H_{tide} \simeq 8.10^{-6} \text{ W.m}^{-3}$) are obtained toward the poles and minima ($H_{tide} \simeq 2.10^{-6} \text{ W.m}^{-3}$) at the equator (in agreement with Ojakangas and Stevenson [1989]).

[20] For an incompressible Maxwell medium, subjected to sinusoidal variation of strain rate $\dot{\epsilon}_{ij}$, the average volumetric dissipation rate H is

$$H = \frac{2\eta\dot{\epsilon}_{ij}^2}{1 + (\omega\eta/\mu_E)^2} \quad (12)$$

Table 1. Physical Parameters of Europa's Interior Model

Layer	R_{min} – R_{max} , km	ρ , kg.m $^{-3}$	μ_E , GPa	K, GPa	η , Pa.s
Iron core	0–650	5500	0	550	0
Silicate mantle	650–1415	3500	70	130	10^{21}
Ocean	Z_{O^I} ^a	1000	0	2.25	0
Ice shell	Z_{O^I} ^a –1565	920	3.3	10	$\eta(z) = f(T(z))$ ^b

^aDepth of the ocean-ice interface.

^bViscosity profile given by the thermal convection numerical model.

A peak of dissipation occurs when $\omega\eta/\mu_E = 1$, i.e., when $\eta \simeq 10^{14}$ Pa.s. Such a relationship can be rewritten as

$$H = \frac{2H_{max}}{\eta/\eta_{max} + \eta_{max}/\eta} \quad (13)$$

where $H_{max} = \mu_E \dot{\epsilon}_{ij}^2 / \omega$ is the maximum of volumetric dissipation rate that occurs at a viscosity $\eta_{max} = \mu_E / \omega$. Figure 2 shows the good fit of tidal dissipation rate computed from the radial functions of Europa with tidal dissipation rate calculated with the previous formula (equation (13)), within the ice shell. This implies that tidal strain rate $\dot{\epsilon}$ averaged over one tidal cycle is nearly constant through the ice layer and that tidal dissipation mainly depends on the viscosity profile in the ice layer. On Figure 3, the tidal heating rate calculated with equation (13) is plotted for two extreme values expected for H_{max} within Europa's ice shell, corresponding to the tidal strain rates $\dot{\epsilon} = 10^{-10}$ and $2.10^{-10} \text{ s}^{-1}$. For ice viscosity lower than 10^{17} Pa.s, tidal heating rate is larger than the radiogenic heating rate in the silicate mantle.

[21] Convective instabilities in the ice shell create lateral viscosity variations. Such lateral variations should have a small effect on the tidal strain rate. On the other hand, if the mean tidal strain rate is locally constant within the ice layer, the tidal dissipation rate per unit volume will depend on both lateral and radial viscosity variations. Since equation (13) reproduces well the radial distribution of tidal dissipation in the ice shell, we assume that it also provides a good assessment of the lateral variations of tidal dissipation due to convective instabilities. Thus the tidal heating rate field $H_{tide}(x,z)$ is computed at each time step from the viscosity field $\eta(x,z)$ for a given set of H_{max} and η_{max} .

2.4. Partial Melting

[22] After each timestep dt , temperature T^* predicted from the dynamical equations is compared to the melting temperature T_m . If T^* exceeds T_m , T is set to T_m and the corresponding amount of melt production δx_m is calculated. Inversely, if T^* is lower than T_m and melt fraction x_m is not zero, T is set to T_m and the corresponding amount of melt crystallization is calculated.

$$\delta x_m = \frac{c_p}{L} (T^* - T_m), \delta x_m > 0 \text{ if } T^* > T_m \Rightarrow T = T_m, \\ \delta x_m < 0 \text{ if } T^* < T_m \text{ and } x_m > 0 \Rightarrow T = T_m, \quad (14)$$

where c_p is the heat capacity of ice, L is the latent heat of melting for pure water ice (see Table 2).

[23] Liquid water appears in veins at the junctions of three or four grains, and in lenses in grain boundaries (see Nye [1989] for a detailed description of this system). For low dihedral angle characteristic of the ice-water system: $\theta_{dh} = 20\text{--}30^\circ$ [Hobbs, 1974], melt/solid configuration allows the connectivity of the liquid phase even at small melt

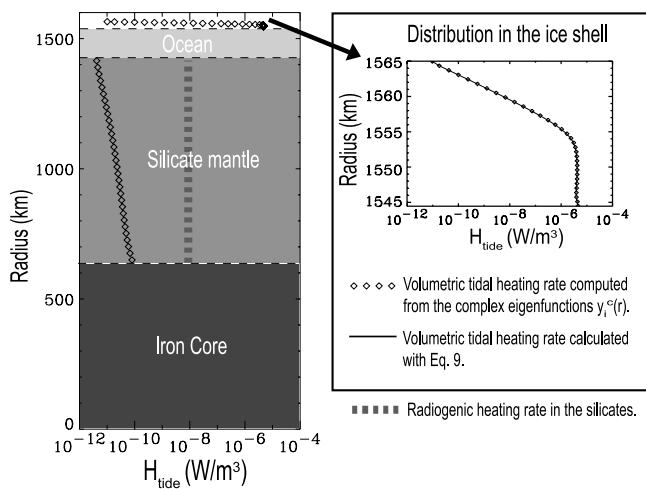


Figure 2. Radial distribution of tidal heating within Europa and detailed distribution in the ice layer. Tidal dissipation is computed from the complex eigenfunctions $y_i^c(r)$ of Europa's interior, for the internal structure model described in Table 1 and Figure 1. The viscosity in the ice layer is calculated from the temperature profile obtained without tidal heating. The radiogenic heating rate per unit volume is also displayed as a comparison. The detailed distribution in the ice layer presents a comparison between the tidal heating obtained by integration of the eigenfunctions $y_i^c(r)$ and the tidal heating given by equation (13). The good agreement between the two plots shows that the radial distribution of tidal heating in the ice shell is mainly controlled by the ice viscosity profile. This indicates that the strain rate does not vary with depth in the ice shell.

fractions. However, when a small non-hydrostatic stress is applied (~ 0.1 MPa), water lenses appear [Nye and Mae, 1972]. In the tidally stressed conditions of Europa's ice shell [Greenberg et al., 1998], we may ask whether such water

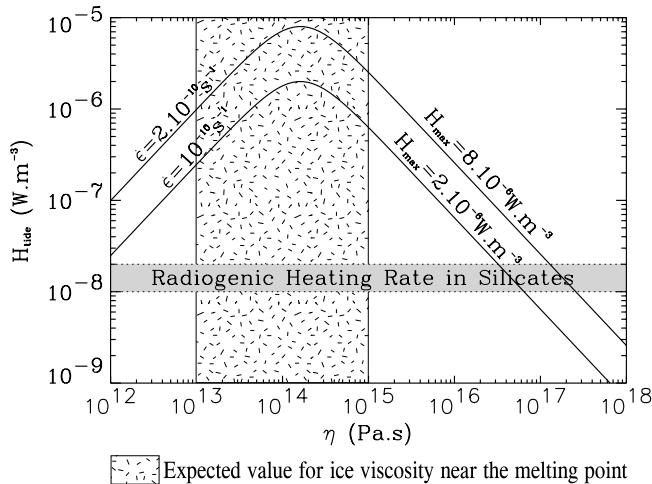


Figure 3. Volumetric tidal heating rate within Europa's ice shell as a function of ice viscosity, calculated with equation (13) for two extreme values of tidal strain rate: $\dot{\epsilon} = 2.10^{-10} \text{ s}^{-1}$ near the poles and $\dot{\epsilon} = 10^{-10} \text{ s}^{-1}$ at the equator. For viscosities lower than $5.10^{16}\text{--}10^{17} \text{ Pa.s}$, tidal heating rate per unit volume is larger than the radiogenic heating rate per unit volume of the silicate mantle.

Table 2. Physical Parameters of Ice I

Physical Quantity	Symbol	Unit	Value
Density ^a	ρ	kg/m^3	920
Thermal conductivity ^a	k	W/m/K	2.3
Thermal diffusivity ^a	κ	m^2/s	1.2×10^{-6}
Thermal expansion ^a	α	K^{-1}	1.6×10^{-4}
Latent heat of fusion ^a	L	kJ/kg	300
Heat capacity ^a	c_p	J/kg/K	2100
Viscosity at the melting point ^b	η_m	Pa.s	$10^{13}\text{--}10^{15}$
Activation energy ^b	E	kJ/mol	50

^aThese physical parameters are estimated at $T = 270\text{K}$ from Hobbs [1974].

^bViscosity and activation energy are discussed in section 2.2.

lenses will form, with corresponding constrictions of the veins, and will reduce the permeability of ice to water.

[24] In the present study, we assumed that melt transport by percolation is not efficient because of the small amount of melt ($\leq 2\%$) and that the liquid phase may not be interconnected. The retention of water in ice has two major effects. First, it modifies the buoyancy of ice. The density change $\delta\rho_m$ due to melt fraction is included in the dynamical equations:

$$\delta\rho_m = x_m\rho_i(1 - \rho_i/\rho_w) \quad (15)$$

where ρ_i is the density of pure water ice and ρ_w is the density of pure water, creating a negative buoyancy term \vec{f}_{melt} (equation (2)). Second, the presence of melt decreases the viscosity of ice (equation (8)).

2.5. Numerical Model

[25] We consider a Cartesian domain with reflecting side boundaries. A free-slip condition is assumed for the upper and lower boundaries. The numerical program uses a finite difference method on a staggered grid mesh for solving both the flow equations (equation (1) and equation (2)) and the conservation of energy (equation (3)). Continuity and conservation of momentum are solved for each temperature timestep with a multi-grid scheme adapted to large viscosity gradients. A simple scheme minimizing numerical diffusion is used for the advection of temperature and melt fraction [Smolarkiewicz, 1984]. At each temperature timestep, the melt production or crystallization is calculated. The aspect ratio is 2, and the number of grid points is 256 in the horizontal direction and 128 in the vertical direction. Numerical experiments are performed for prescribed Rayleigh number and increasing values of dimensionless maximal tidal heating h_{max} , for three different bottom viscosity values: $\eta_{bot} = \eta_{max}/4$, η_{max} or $4 \times \eta_{max}$.

3. Model Results

3.1. Detailed Description of One Numerical Experiment

[26] Figure 4 presents a snapshot of the temperature and tidal heating fields obtained with our 2D thermal convection model and dimensionalized for $\Delta T = 170\text{K}$, $T_{bot} = 270\text{K}$ and $\eta_{bot} = \eta_{max} = 1.5 \times 10^{14} \text{ Pa.s}$. The Rayleigh number Ra_{bot} is equal to 1.68×10^6 and the dimensionless maximal tidal heating h_{max} is 3. With the above value of Ra_{bot} and parameters displayed in Table 2, this corresponds to a thickness $b = 20\text{km}$ and to a maximal tidal heating rate $H_{max} = 2.7 \times 10^{-6} \text{ W.m}^{-3}$. Tidal heating (Figure 4b) is mainly located in the bottom half of the ice shell where

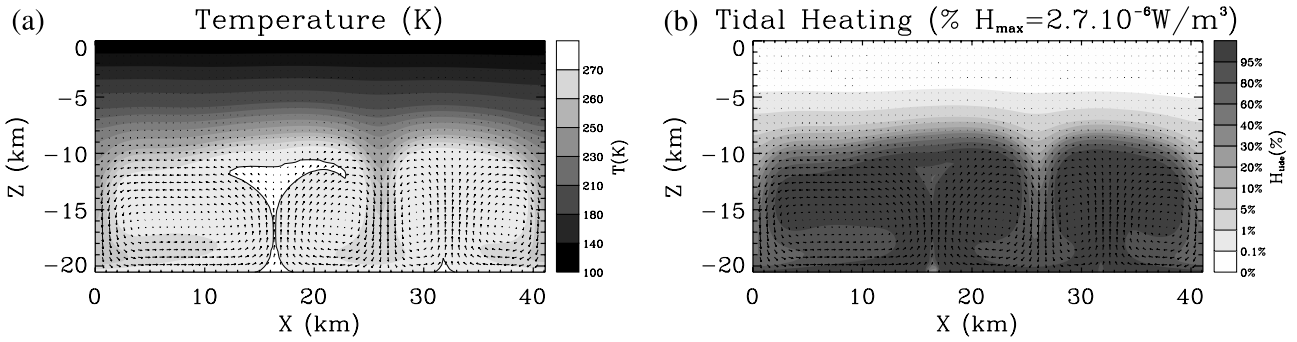


Figure 4. Temperature (a) and tidal heating rate per unit volume (b) fields obtained for the following parameters: ice shell thickness $b = 20$ km, bottom temperature $T_{bot} = T_m = 270$ K, bottom viscosity $\eta_{bot} = \eta_{max}$ and viscosity ratio $\Delta\eta = 1.2 \times 10^6 \Leftrightarrow \gamma_T = 14$, tidal heating parameters: $H_{max} = 2.7 \times 10^{-6}$ W/m³ and $\eta_{max} = 1.5 \times 10^{14}$ Pa.s. The black isocontour delimits the area where temperature equals to the melting temperature of pure water ice.

temperature is relatively close to the melting temperature. Since $\eta_{bot} = \eta_{max}$ is prescribed, the maximal heating occurs in hot plumes. In the convective sublayer, the lateral variations of the tidal heating rate reach values of 40–60% of H_{max} . A maximum of 80% is obtained at the top of hot plumes. Lateral variations of temperature δT_x are ~ 10 K in the convective sublayer and ~ 20 K at the top of hot plumes. The melting temperature is reached at the center of the hot plume on the left. The black isocontour delimits the region where partial melting occurs ($x_m > 0$).

3.1.1. One-Dimensional Description of the Different Sublayers in the Ice Shell

[27] Figure 5 shows the corresponding horizontally averaged temperature profile (a) and the advective and diffusive heat flux profiles (b), averaged through time. All the numerical experiments considered in the present study are within the conductive lid regime. The thermal structure can be described by the following five parameters: z_{lid} , z_{CTBL} , z_{HTBL} , z_{lid} , and T_i . z_{lid} is the thickness of the conductive lid, computed from the advective flux (Figure 5b, black curve): it is the depth at which the tangent to the advection

profile at the upper inflection point intersects the y-axis. T_{lid} (Figure 5a) is the horizontally averaged temperature at this depth. T_i is the temperature of the well-mixed interior (volumetric average of the temperature profile between the depth of the upper local maximum (z_{max}) and the depth of the lower local minimum (z_{min})). z_{CTBL} is the depth of the base of the cold thermal boundary layer, such that:

$$z_{CTBL} - z_{lid} = \frac{k(T_i - T_{lid})}{\phi_{lid}}, \quad (16)$$

where ϕ_{lid} is the diffusive heat flux at $z = z_{lid}$. z_{HTBL} is the depth of the top of the hot thermal boundary layer, such that:

$$b - z_{HTBL} = \frac{k(T_{bot} - T_i)}{\phi_{bot}}, \quad (17)$$

where ϕ_{bot} is the heat flux at the base of the ice shell ($z = b$).

3.1.2. Effect of Tidal Heating

[28] Similar profiles, obtained for a simulation with the same parameters but without any tidal heating, are plotted

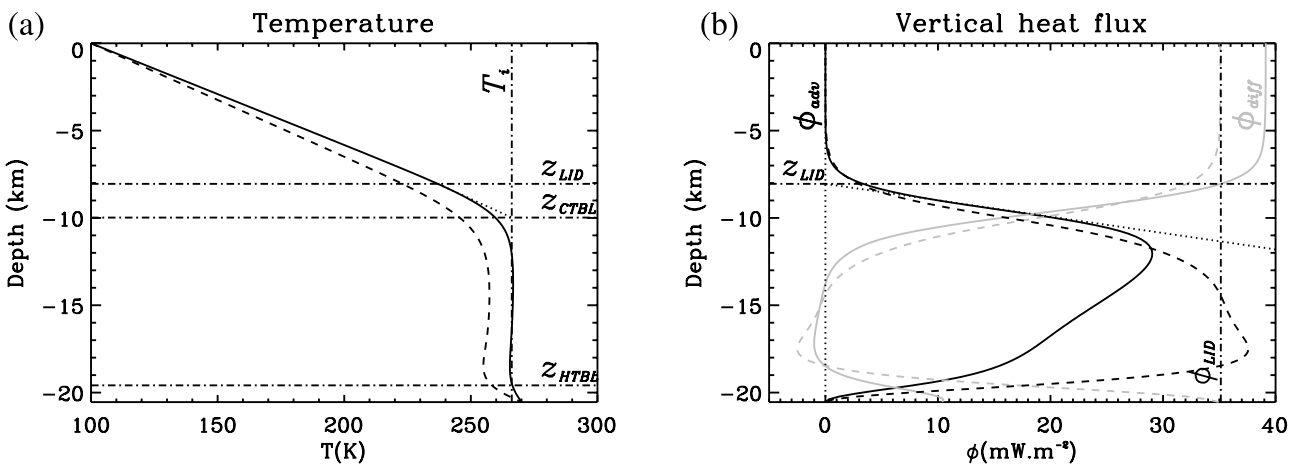


Figure 5. Horizontally averaged temperature (a) and, horizontally averaged vertical diffusive and advective heat fluxes (b) corresponding to Figure 4 (solid line). The dashed lines correspond to results obtained with the same parameters but without tidal heating. The five parameters z_{lid} , z_{CTBL} , z_{HTBL} , z_{lid} , and T_i describing the thermal structure are indicated. The bottom heat flux strongly decreases when tidal heating is added, while the surface heat flux and the conductive lid thickness do not vary significantly.

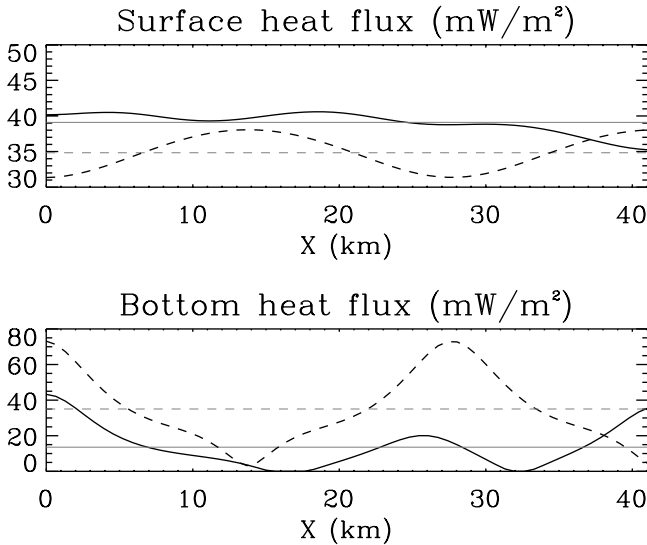


Figure 6. Surface and bottom heat fluxes corresponding to Figure 4 (solid line), and to the same run without tidal heating (dashed line).

for comparison. This shows that although tidal heating increases the temperature T_i of the well-mixed interior (and consequently decreases the temperature difference across the hot thermal boundary layer), the thickness of the conductive lid z_{lid} remains nearly constant: $z_{lid} \simeq 8$ km (Figure 5a).

[29] The instantaneous surface and bottom heat fluxes, corresponding to Figure 4, as well as their horizontal average are plotted as a function of the horizontal coordinate X on Figure 6. Since the bottom temperature T_{bot} is prescribed, the addition of volumetric (tidal) heating induces a large decrease ($\sim 60\%$) of the average bottom heat flux and a small increase ($\sim 10\%$) of the average surface heat flux. This can be also seen on Figure 5b. The addition of laterally heterogeneous heat sources reduces the lateral variations of surface heat flux and the advective heat flux in the bottom part of the layer.

3.1.3. Heat Flux

[30] Figure 7 shows the time evolution of the horizontally averaged surface and bottom heat fluxes ϕ_{surf} and ϕ_{bot} (Figure 7b), the volumetrically averaged tidal heating rate $\langle H \rangle$ (Figure 7a) and the volumetrically averaged partial melt $\langle x_m \rangle$ (Figure 7c). The bottom heat flux ϕ_{bot} is strongly time-dependent: it ranges from a 15 mW.m^{-2} maximum to a zero value corresponding to a large amount of melt present in the bottom part of the convective sublayer. On the contrary, the surface heat flux ϕ_{surf} varies very weakly. Due to the slow heat transfer through the thick conductive lid (40% of the total layer), the time variations of surface heat flux are smoothed as well as its lateral variations (Figure 6).

3.1.4. Partial Melt

[31] The time evolutions of $\langle H \rangle$ and $\langle x_m \rangle$ (Figures 7a and 7c) are clearly correlated. An increase of the average tidal heating $\langle H \rangle$ induces an increase of the average amount of partial melt $\langle x_m \rangle$ with a small delay. This in turn reduces the total amount of tidal heating by decreasing locally the viscosity of ice (see Figure 4b).

[32] Figure 8 displays four successive snapshots of the melt distribution within the convective sublayer. The first one (Figure 8a) corresponds to the same time than the temperature and tidal heating fields on Figure 4. The time interval between the first snapshot (Figure 8a) and the last one (Figure 8d) is indicated by two vertical dashed lines on the $\langle x_m \rangle$ plot (Figure 7c). At $t = 0$ (Figure 8a), partial melt is mainly located at the top of an upwelling hot plume, with a maximum amount of about 1.5%. The fusion of ice in hot plumes uses about 10% of the total tidal heating of the ice layer because of latent heat. After 45000 years (Figure 8b), the melt fraction has faintly increased up to about 2%, and inhibits the upwelling, because water is denser than ice. Assuming that melt is not extracted, the presence of water creates negative buoyancy which overcomes the thermal buoyancy and leads to a rapid downwelling. After 90,000 years (Figure 8c), the velocity of the partially molten hot plume is reversed dragging colder solid ice with it. Finally,

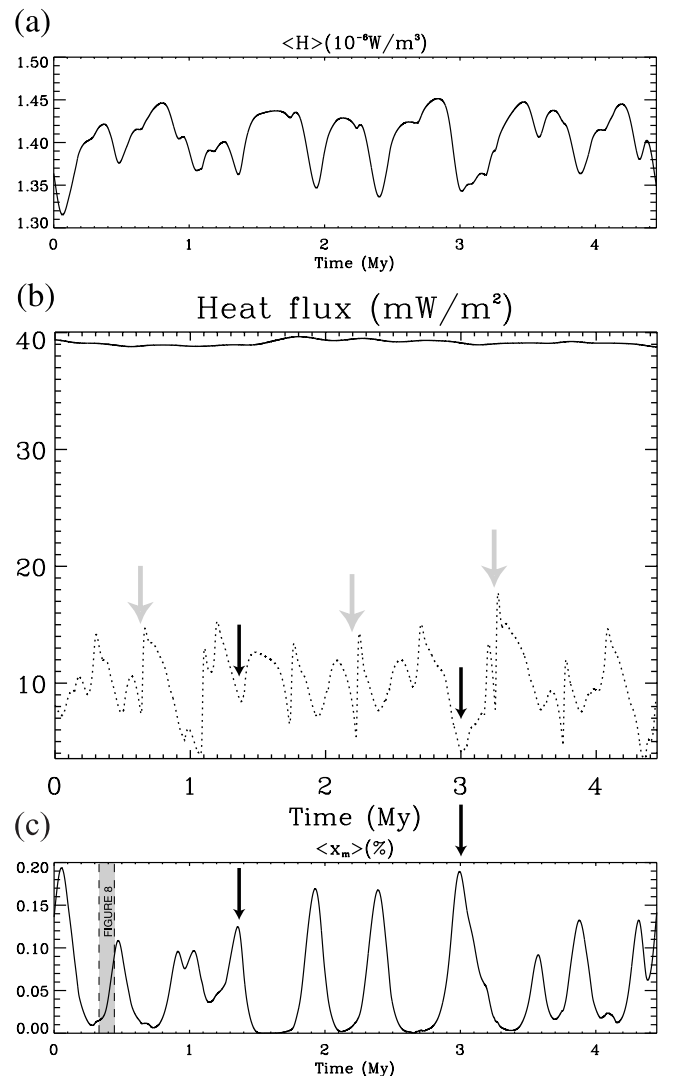


Figure 7. Time evolution of the volumetric average tidal heating rate $\langle H \rangle$ (a), of the horizontal average of the bottom (dotted line) and surface (solid line) heat fluxes (b), and of the volumetric average partial melt $\langle x_m \rangle$ (c), for the simulation corresponding to Figure 4.

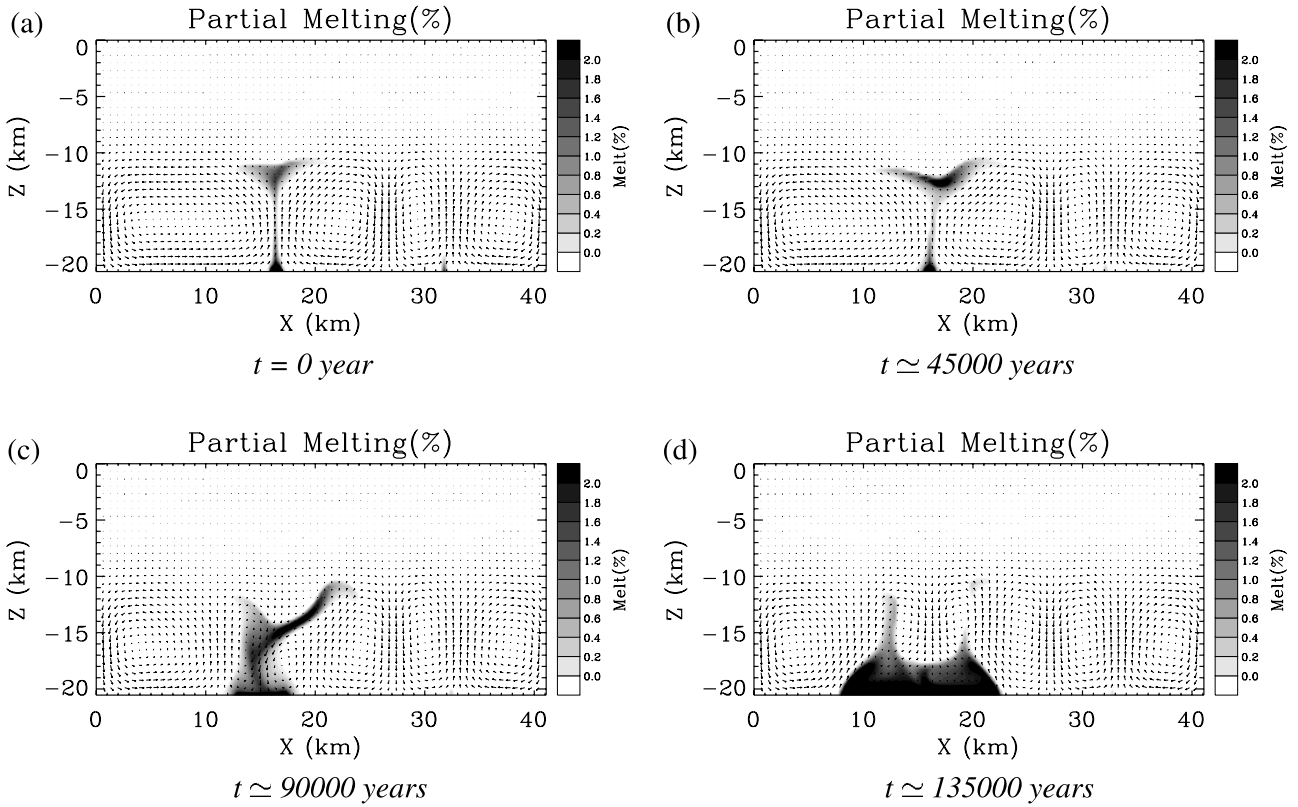


Figure 8. Time evolution of partial melt distribution within the ice shell for the run corresponding to Figure 4. The occurrence of partial melting in hot plumes leads to episodic upwellings of partially molten ice up to the base of the conductive lid. The residence time of partial melt at the top of hot plumes is around 50,000 years.

after 135,000 years (Figure 8d), a large amount of partial melt accumulates at the base of the vanished hot plume. For this numerical experiment, the residence time of partially molten ice in the head of a hot plume is around 50,000 years. Then, partial melt accumulated at the base of the ice shell disappears gradually. From Figure 7c, it is shown that the averaged partial melt $\langle x_m \rangle$ become almost zero after about 100,000–150,000 years. All other partial melting episodes observed in our calculations have approximatively the same characteristics. The time interval between two episodes is about 0.5 Ma. Note that the positive buoyancy of hot plumes vanishes because the present models assume melt retention in the ice matrix. If melt percolates downward efficiently, water would drag the hot plumes, but may not annihilate them. In all cases, partial melting will occur at the top of the hot plumes, and the solutions will be probably time-dependent. Implications for the formation of chaotic terrains are discussed in the next section.

[33] An increase of partial melt always induces a decrease of the averaged bottom heat flux (indicated by black arrows on Figure 7), and locally the presence of partial melt completely annihilates the bottom heat flux (see Figure 6a and Figure 8a at $X = 15$ – 18 km). The downwelling of cold solid ice dragged by the partially molten material explains the large and rapid increase of the bottom heat flux (see gray arrows on Figure 7), when it reaches the bottom of the ice shell.

[34] It is noteworthy to emphasize that the occurrence of partial melting is clearly responsible of the time-dependency

of the system dynamics as demonstrated by Figure 7 and Figure 8. For runs with the same Rayleigh number but for a smaller value of tidal heating, the melting point is not reached and the convective solution is steady.

3.2. Effect of the Value of Bottom Viscosity η_{bot}

[35] In order to study the influence of the bottom viscosity η_{bot} , Figure 9 presents the temperature and the associated tidal heating fields obtained for a four times smaller value of η_{bot} (all the other parameters remaining the same than those used for Figure 4). Lower viscosity enhances the vigor of convection (four times larger Rayleigh number). Consequently, the surface heat flux ϕ_{surf} is higher and the conductive lid thinner. The maximal tidal dissipation now occurs at the top of the convective sublayer and in cold plumes (Figure 9b). Nevertheless, a significant part of the tidal dissipation still takes place in hot plumes (tidal heating reaches at least a value of 40% of the maximum tidal heating). Since the convective sublayer is thicker than the one corresponding to Figure 4, the volumetrically averaged tidal heating averaged through time $\langle H \rangle_t$ is almost the same. Its effect on surface and bottom heat fluxes compared to a case without tidal heating is similar. Since heat transfer is more efficient, the increase of the temperature of the well-mixed interior T_i is smaller. In addition, the amount of tidal heating in hot plumes is smaller, so that the melting temperature is never reached.

[36] Although no partial melting occurs within the ice layer, the solution is time-dependent with smaller variations

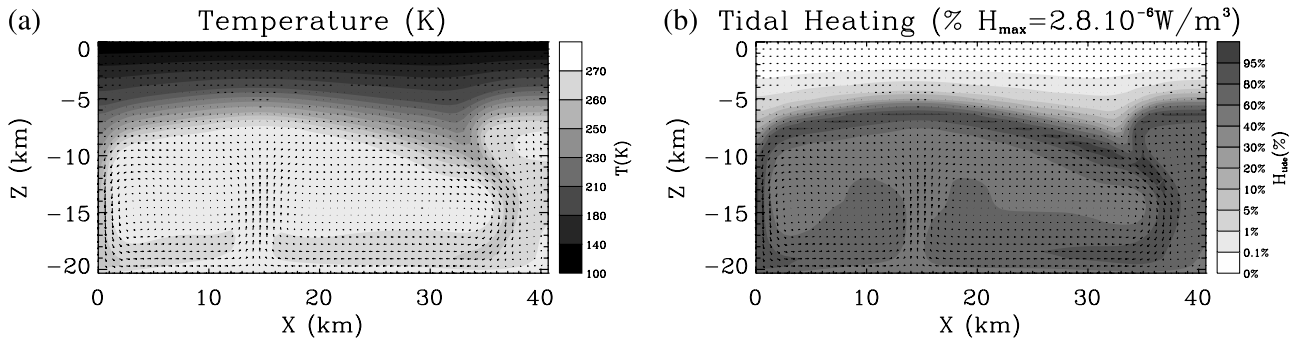


Figure 9. Same as Figure 4 but with $\eta_{bot} = \eta_{max}/4$. The maximal tidal dissipation (b) occurs in the cold boundary layer and in cold plumes. The convective sublayer is thicker than in Figure 4, but the temperature in hot plumes does not reach the melting point.

of ϕ_{bot} . Contrary to the case presented before with a smaller value of Rayleigh number, tidal heating itself provides the conditions for the time-dependence, which is a well-established fact in the case of homogeneous internal heat sources [Parmentier et al., 1994] (see also Schubert et al. [2001a] for a review).

[37] Simulations for a bottom viscosity four times higher than η_{max} : $\eta_{bot} = 6.10^{14}$ Pa.s (not shown here) have also been performed. For an ice shell thickness of 20 km, the Rayleigh number is too small to allow convective motion, heat is transferred by thermal diffusion only. This bottom viscosity value reduces the amount of tidal heating, since the maximum value is never reached within the layer's viscosity range ($\eta_{bot} > \eta_{bot}$). The viscosity value has a very strong influence. If it is too small compared to the optimum value η_{max} , no melting is obtained. If it is too large, convection is not efficient enough. It is interesting to note that the optimum value η_{max} of viscosity is in the range of viscosity one can expect from laboratory studies.

3.3. Effect of the Value of Maximal Tidal Dissipation H_{max}

[38] The effect of the addition of tidal heating has already been mentioned (Figure 5). Maximal tidal heating rate H_{max} further controls the presence and the amount of partial melt. Table 3 summarizes the observed critical value of $H_{max,cr}$ for partial melting to occur. For a given value of bottom viscosity η_{bot} , $H_{max,cr}$ decreases with the thickness of the layer. When η_{bot} is different from η_{max} , a higher value of $H_{max,cr}$ is needed to induce partial melting.

[39] Figure 10 shows the tidal heating and the partial melt fields obtained for a H_{max} value higher than on Figure 9 ($H_{max} = 4.6 \times 10^{-6}$ W.m⁻³, all the other parameters remaining the same as Figure 4). The buoyancy of the partially molten hot plumes is reduced, however since the upwelling velocity is larger and the amount of melt present is smaller, the hot plumes are not reversed. At the top of a hot plume, the partially molten ice is advected horizontally, and re-crystallizes progressively.

3.4. Heat Transfer

[40] Figure 11 summarizes heat flux results obtained for two different ice layer thickness values b (15 and 20 km) and two different bottom viscosity values η_{bot} ($\eta_{bot} = \eta_{max}/4$ and $\eta_{bot} = \eta_{max}$) as functions of the maximal tidal heating rate H_{max} . An assessment of the heat flux out of the silicates,

including radiogenic decay and secular cooling, is also indicated. The lower bound of this heat flux corresponds to the case where the heat flow is in equilibrium with the radiogenic heat production in the silicate mantle. The present-day radiogenic heating rate in the silicate mantle would be between about 1.5 and 2.10^{11} W, depending on its thickness and on its composition. However, a large temperature ($T_{sil} > 1200$ –1400 K) of the silicate mantle is required for the initiation of convection. Such a temperature may be reached relatively late in the thermal evolution of Europa [Grasset et al., 2000]. If mantle convection starts after 2–3 Gy, it is currently still evacuating radiogenic heat accumulated during the 2–3 first billion years. A large part of the present-day surface heat flow would then come from the cooling of the silicate interior, and could be as high as 20 mW.m⁻².

[41] A systematic result is that the bottom heat flux ϕ_{bot} decreases continuously and significantly when H_{max} increases, down to the value of the heat flux from the silicate mantle and lower, while the surface heat flux ϕ_{surf} increases very slowly. The conductive lid thickness z_{lid} mainly varies with the bottom viscosity η_{bot} , and remains almost constant as tidal heating increases. The main effect of tidal dissipation is to reduce the ability of the ice shell to transfer heat from the interior toward the surface. When tidal dissipation and/or ice shell thickness increase, the ice layer becomes less and less efficient to cool the subsurface ocean.

4. Discussion

4.1. Thickness of an Ice Shell in Convective Equilibrium

[42] The equilibrium thickness of the ice shell can be derived from the results presented in Figure 11 as a function of the maximal dissipation H_{max} . Assuming that the heat

Table 3. Critical H_{max} Value for the Occurrence of Partial Melting in Hot Plumes^a

	$\eta_{bot} = \eta_{max}/4$	$\eta_{bot} = \eta_{max}$	$\eta_{bot} = 4 \times \eta_{max}$
$b = 15$ km	6.10^{-6}	3.10^{-6}	no convection
$b = 20$ km	4.10^{-6}	2.10^{-6}	no convection
$b = 25$ km	3.10^{-6}	1.5×10^{-6}	$3.3.5 \times 10^{-6}$
$b = 35$ km	$2-2.5 \times 10^{-6}$	10^{-6}	2.10^{-6}

^aUnits are W.m⁻³.

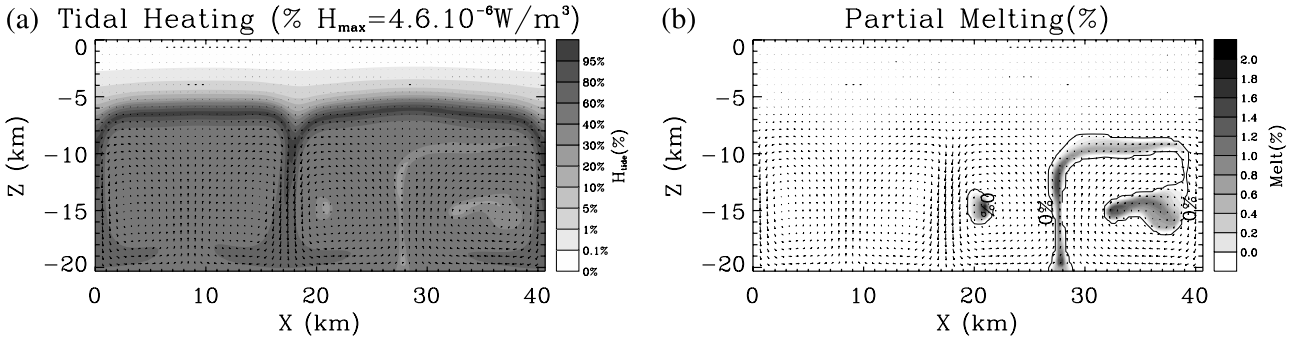


Figure 10. Same as Figure 9 but with a higher value of H_{max} ($4.6 \times 10^{-6} \text{ W/m}^3$). In this case, partial melting occurs in hot plumes and modifies their dynamics.

flux from the silicate interior is equal to 10 mW.m^{-2} and $\eta_{bot} = \eta_{max}$, it follows from Figure 11b that a H_{max} value of about $5.10^{-6} \text{ W.m}^{-3}$ is required to get a steady heat transfer for a 15 km thick ice shell (a value of about $2.5 \times 10^{-6} \text{ W.m}^{-3}$ is required for a 20 km thick ice shell). From all equilibrium values obtained with our numerical results, the thickness b for which $\phi_{bot} = \phi_{sil} = 10 \text{ mW.m}^{-2}$ can be

derived as a function of H_{max} , by interpolating linearly all the results. Thus a map of the equilibrium thickness of the ice shell can be obtained from Europa's map of the maximal tidal dissipation (H_{max}) calculated from the dissipation model (see section 2.3).

[43] Two major corrections must be taken into account to accurately assess the “real” thickness of the ice shell:

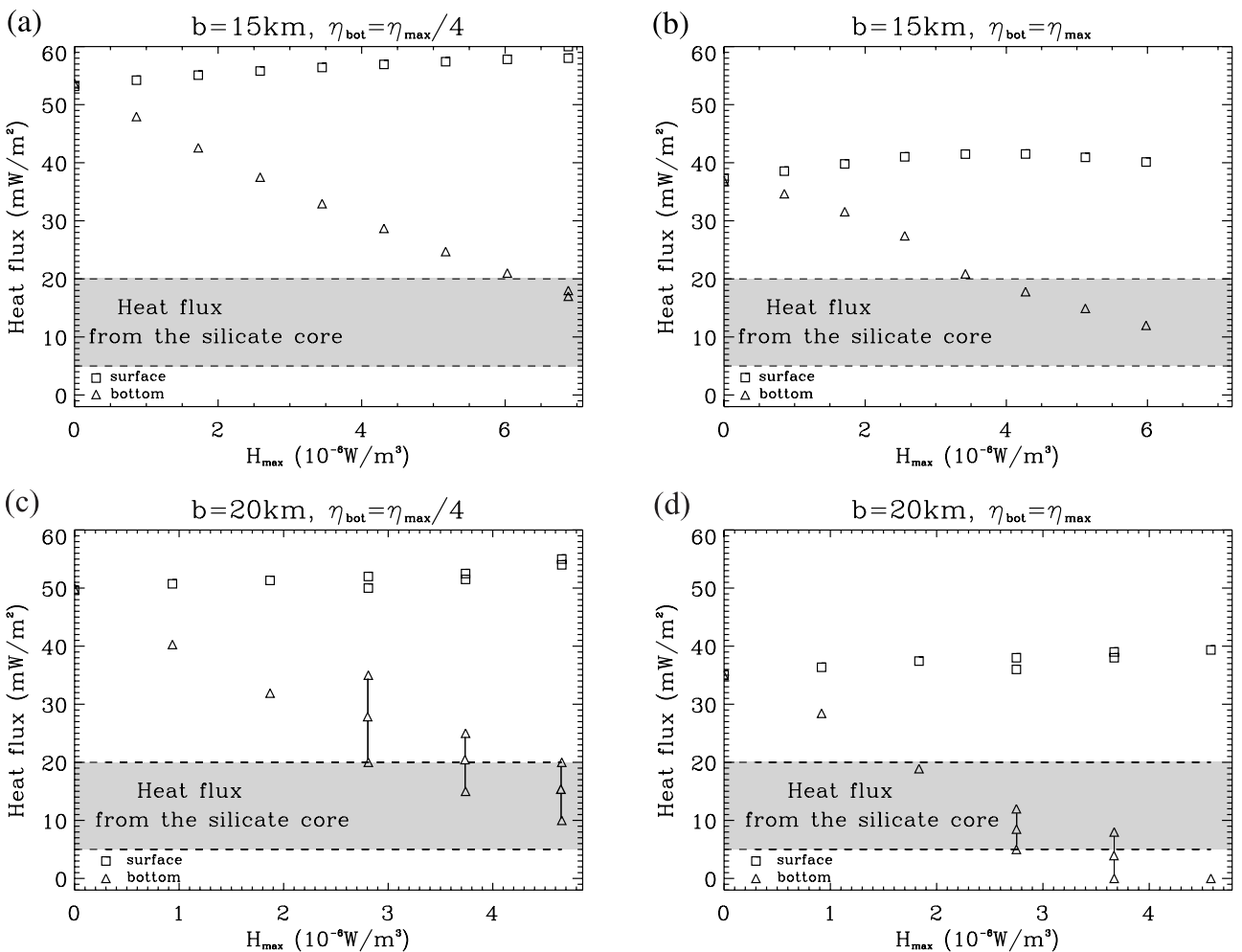


Figure 11. Horizontally averaged heat flux at the base (triangle) and at the surface (square) of the ice shell as a function of the maximal tidal dissipation rate H_{max} for two different ice shell thicknesses (b) and two different bottom viscosity values (η_{max}). An assessment of the heat flux from the silicate core is indicated in grey.

temperature-dependent conductivity and latitude-dependent surface temperature.

[44] Our models of thermal convection are performed with a constant value of thermal conductivity k (evaluated at $T = 270\text{K}$), whereas the thermal conductivity of ice is temperature-dependent: $k(T) = 488.12/T(\text{K}) + 0.4685$ [Hobbs, 1974]. We assume that this has a minor effect on heat transfer in the convective sublayer, and results mainly in the thickening of the conductive lid where the temperature gradient is maximal. The detailed calculation of a more realistic value of the conductive lid thickness is presented in Appendix A.

[45] Second, the surface temperature is related to the annual average solar insolation, which varies largely with latitude. Following Ojakangas and Stevenson [1989], the surface temperature T_{surf} is calculated as:

$$T_{surf}(\theta) = \left[\frac{(1-A)}{\sigma_s} (\pi F_s) \left(\frac{\cos(\theta)}{\pi} \right) \right]^{1/4}, \quad (18)$$

where θ is the latitude ($-85^\circ \leq \theta \leq 85^\circ$), A is the albedo of the ice ($A \simeq 0.5$), σ_s is the Stefan-Boltzmann constant ($\sigma_s = 5.7 \times 10^{-8} \text{ W.m}^{-2}\text{K}^{-4}$), and πF_s is the solar flux at Jupiter's orbit ($\pi F_s \simeq 50 \text{ W.m}^{-2}$). It results that the surface temperature varies between 110K at the equator to 60K near the poles. For each value of surface temperature T_{surf} , a different relationship between the equilibrium thickness b_{eq} and the maximal tidal heating rate H_{max} is derived. The details of the dimensionalization and of the derivation of $b = f(H_{max})$ are presented in Appendix B. We define a thickening coefficient x_{lid} which is the ratio between the corrected thickness of the conductive lid and the thickness obtained with thermal convection models with a constant conductivity. This coefficient x_{lid} depends on the surface temperature, and must be estimated for different values of the surface temperature.

[46] Figure 12a shows the distribution of the corrected ice shell thickness e_{ice} over the surface of Europa due to the variations of H_{max} (section 2.3) and of T_{surf} , assuming $\eta_{max} = \eta_{bot}$ and $\phi_{sil} = 10 \text{ mW.m}^{-2}$. The maximal thickness is obtained where the tidal heating is minimal, i.e., on both sides of the equator at the sub-Jovian and anti-Jovian points ($\lambda = 0^\circ$ and $\lambda = 180^\circ$, respectively). The minimal thickness is not found at the poles where the maximal dissipation occurs, but at midlatitudes. This is a consequence of the latitudinal variations of the surface temperature T_{surf} . Two effects are responsible for the thickening of the ice shell toward the poles. First, a higher value of the temperature variation ΔT through the ice layer tends to increase the effective equilibrium thickness b_{eq} . Second, the conductive lid is all the more thickened than the surface is cold. This leads to globally averaged values of 22 km for the corrected thickness of the whole layer e_{ice} and of 12 km for the conductive lid z_{lid} .

[47] Another consequence of the surface temperature variation is to modify strongly the depth of a given isotherm. Figure 12d shows the map of the depth of the 200K isotherm. Note that this isotherm does not coincide with the base of the conductive lid (Figure 12b) and that it is 1.5 times deeper toward the poles (~ 13 km) than at the equator (~ 9 km). These latitudinal variations will probably

affect the estimate of the elastic thickness of the ice layer, subjected to tidal flexing. The mechanical behavior of the ice shell at the poles will be probably different from the one at the equator.

4.2. Variations of the Equilibrium Thickness

[48] Several parameters prescribed in our calculation may affect the mean value and the lateral variations of the ice shell thickness we derive.

[49] 1. Bottom viscosity value η_{bot} . For smaller viscosity value, Figures 11a–11c show that a larger equilibrium thickness is found. An average corrected thickness value of 25–26 km is expected, whose conductive lid is 10.5-kilometers thick. The lateral thickness variations remain almost the same.

[50] 2. Heat flux from the silicate interior ϕ_{sil} . For $\phi_{sil} = 5 \text{ mW.m}^{-2}$, the average ice shell thickness is equal to 23.5 km, i.e., 1.5 km more than for $\phi_{sil} = 10 \text{ mW.m}^{-2}$. For $\phi_{sil} = 20 \text{ mW.m}^{-2}$, the equilibrium thickness is so thin that convection vanishes almost everywhere except at locations near the equator. For a higher bottom heat flux, the entire ice shell is conductive. Lateral variations of ϕ_{sil} at the lower surface of the ice may affect locally the equilibrium thickness. Such variations may be significant in the case of episodic ocean megaplumes generated by hotspots on the sea floor [Thomson and Delaney, 2001]. However, such conditions would correspond to the case of a very dissipative silicate interior ($\phi_{sil} > 100 \text{ mW.m}^{-2}$), and the ice layer would then be very thin (<5 km) and thus purely conductive.

[51] 3. Surface albedo A . Regional variations of albedo may modify significantly the surface temperature, and consequently the equilibrium thickness. 20% of albedo variations will induce a temperature variation of $\pm 5\text{K}$, which increases or decreases the conductive lid thickness of 10%, corresponding to a thickening (or thinning) of only 3% of the ice layer at the equator.

[52] 4. Maximal tidal dissipation distribution: H_{max} . The lateral variations of the thickness may affect the diurnal tidal flexing of the ice shell as well as the rotation of Europa [Ojakangas and Stevenson, 1989]. A non-synchronous rotation [Geissler et al., 1998] would shift longitudinally the tidal dissipation pattern in Europa's fixed reference, and a more complex tidal flexing would deform the tidal dissipation distribution to some extent. The thickness distribution would be then significantly different. In addition, the variations of the orbital eccentricity e over geological timescales [Hussmann and Spohn, 2002] may also induce time variations of the mean thickness of the ice layer, by modulating the amplitude of the tidal deformation.

[53] 5. Elastic shear modulus μ_E . The value of the elastic shear modulus μ_E of ice at low frequencies is not well constrained. Studies on the tidal bending of the ice shelves on Earth [e.g., Vaughn, 1995] suggest that elastic Young modulus could be about 3 times lower than the one inferred from laboratory measurements. This would decrease by three both H_{max} and η_{max} , so that maximum dissipation would occur in hot plumes for a bottom viscosity value of $4.5 \times 10^{13} \text{ Pa.s}$, instead of a value of $1.5 \times 10^{14} \text{ Pa.s}$. We did not investigate this effect in details, but we expect a larger equilibrium thickness, since tidal dissipation would be smaller and convection more vigorous.

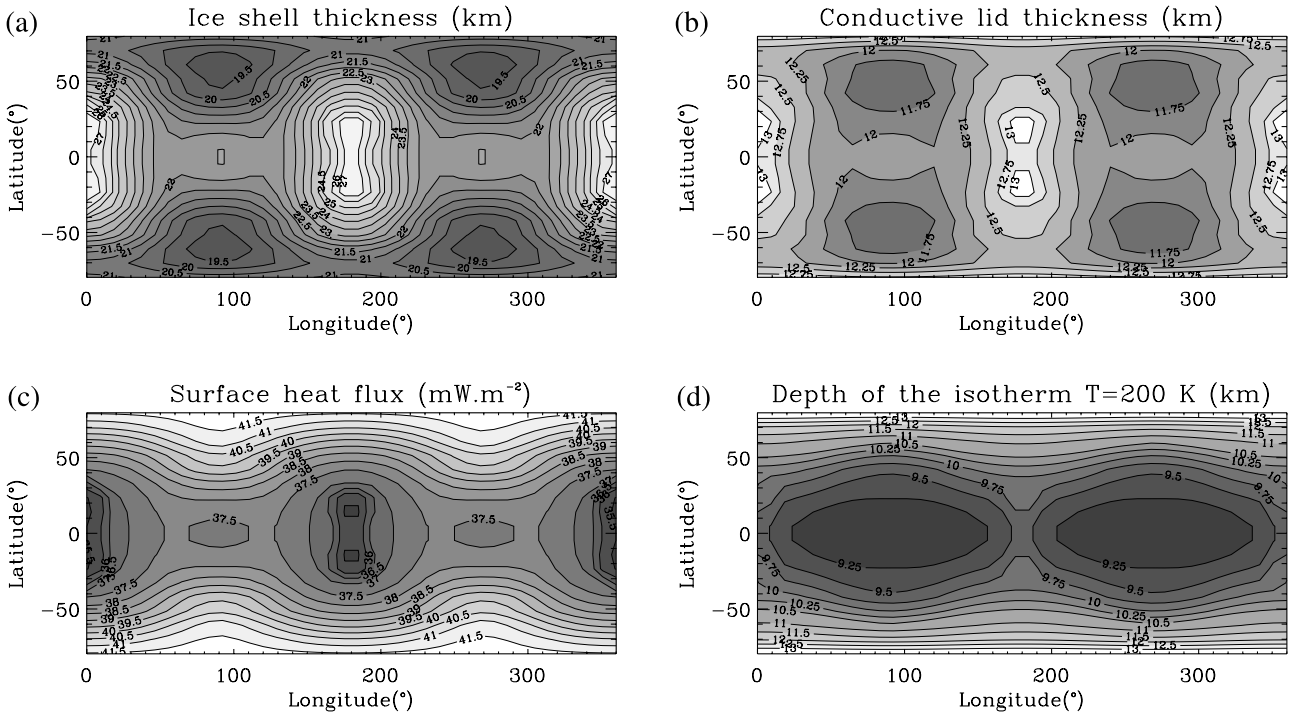


Figure 12. Equilibrium ice shell thickness (a) for a maximal dissipation in hot plumes ($\eta_{max} = \eta_{bot}$) with a heat flux from the silicate core of 10 mW.m^{-2} , and the corresponding conductive lid thickness (b), surface heat flux (c) and depth of the isotherm $T = 200\text{ K}$ (d).

[54] 6. Geometry of the model. All the simulations used to derive the equilibrium thickness are performed with a 2-D Cartesian box with an aspect ratio of 2. One may wonder if this geometry influences the solutions. We performed a few simulations in a 4×1 box, showing very minor differences in the geometry of the plumes and heat transfer budget. Since the thickness of the ice shell is small compared to the radius of Europa ($\sim 1/100$), the use of Cartesian box also seems an acceptable approximation. 3D models might provide different solutions, especially concerning the geometry and size of the hot and cold plumes, as showed in thermal convection modeling (see Schubert *et al.* [2001b] for a review). However, heat transfer should not significantly differ [Travis *et al.*, 1990; Schubert *et al.*, 2001b], so that the equilibrium thickness is probably similar in 3D experiments. The advantage of our 2D approach is to allow a systematical exploration of the parameter space (bottom viscosity η_{bot} , maximal tidal heating H_{max} , etc.).

[55] To sum up, the equilibrium thickness depends mainly on the rheological parameters of ice I. As long as the viscosity near the melting point is relatively close to the optimum value $\eta_{max} = \mu_E/\omega$ for tidal dissipation, an equilibrium thickness with a mean value between 20–30 km is obtained. The value H_{max} of maximal tidal dissipation also controls this thickness, but only large variations of Europa's orbital eccentricity could significantly affect the mean value of the ice shell thickness.

4.3. Total Tidal Dissipation and Surface Heat Flux

[56] Although the average ice shell thickness and its lateral variations are close to the values derived by Ojakangas and

Stevenson [1989] for a purely conductive ice layer with the same bottom heat flux (10 mW.m^{-2}), the global power P_{glob} associated to tidal dissipation is about four times larger, i.e., $P_{glob} \simeq 8.5 \times 10^{11}\text{W}$. The surface heat flux (Figure 12c) varies weakly with latitude in spite of the strong variation of the volumetric tidal dissipation rate ($H_{max} \simeq 8.10^{-6}\text{W.m}^{-3}$ at the poles, and $H_{max} \simeq 2.10^{-6}\text{W.m}^{-3}$ at the equator), which are due to a larger shear strain rate at the poles than the one at the equator. The distribution of tidal heating in the ice shell depends on the Rayleigh number corresponding to the local equilibrium thickness ($Ra_{eq} = 8.10^5$ near the poles, $Ra_{eq} = 1.4 \times 10^6$ at the equator). The vigor of convection controls the radial and lateral extents of the most dissipative ice regions: due to a smaller value of surface temperature, the conductive lid is more thickened at the poles than at the equator. Only the lowermost 35% of the ice shell contributes to the dissipation at the poles, when 50% contributes at the equator.

4.4. Lateral Variations of the Ice Shell Equilibrium Thickness and the Gravity Field

[57] The thickness variations may be responsible for large-scale variations of the gravity field. According to our model, the equilibrium thickness distribution would affect mainly the second and the fourth degrees of the gravity field. At a first order approximation, the lateral thickness variations δe can be described by $\delta e(x) = \delta e_0 \cos(2\pi x/\lambda)$ with $\delta e_0 = 2–3 \text{ km}$, $\lambda = \pi R$. Due to isostatic compensation, this thickness variation will lead to topography variations h : $h(x) = h_0 \cos(2\pi x/\lambda)$, with $h_0 = \delta e_0 (\rho_w - \rho_i)/\rho_w$, ρ_w density of water, and ρ_i density of ice, and to variations of the ocean-ice interface r : $r(x) = \delta e - h = \delta e_0 \frac{\rho_i}{\rho_w} \cos(2\pi x/\lambda)$. The relative

variation of the gravity field measured at a distance z above the surface of Europa can be calculated from these variations:

$$[\delta g/g]_z = \frac{2\pi G}{g} \frac{\rho_i}{\rho_w} (\rho_w - \rho_i) \delta e_0 \cdot \sin\left(\frac{2\pi x}{\lambda}\right) e^{-\frac{2\pi z}{\lambda}} \left[1 - e^{-\frac{2\pi z}{\lambda}}\right] \quad (19)$$

For an orbiter at an altitude of 150 km, $[\delta g/g]_{z=150\text{km}} \simeq 1.5 \times 10^{-6} \sin\left(\frac{2\pi x}{\lambda}\right)$. These variations have almost the same amplitude than the one induced by time-varying tidal potential [Castillo et al., 2000], and could be inferred from an Europa orbiter. However, as it was previously suggested [Ojakangas and Stevenson, 1989; Stevenson, 2000], viscous flow of the bottom warm ice due to the horizontal pressure variations may act in smoothing the ice shell thickness variations to some extent, but they do not totally cancel out the variations [Ojakangas and Stevenson, 1989].

4.5. Partially Molten Ice Plumes, Lenticulae, and Chaos Regions

[58] Another result of interest is the occurrence of partial melting in hot plumes in most of the numerical simulations. From the critical values of H_{max} needed for the initiation of partial melting (Table 3), we show that for an ice shell in equilibrium with a bottom heat flux of 10 mW.m⁻² (Figure 12a), upwelling of partial melt in hot plumes can occur at any place on Europa. These results could have some implications for the formation of the so-called “lenticulae”, which are interpreted as a diapiric intrusion beneath a relatively thin rigid layer [Pappalardo et al., 1998]. Some of these features exhibit disruptions of the surface and evidences of warmer ice extrusions [Fagents et al., 1999]. The rise of partially molten ice in tidally heated hot plumes could explain upbowing, fracturing and melting at shallow depths [Sotin et al., 2002]. Nevertheless, although partial melting in hot plumes is widespread according to our model, the minimal depth of partially molten regions is more than 10 km. Our model predicts thick rigid conductive lids that seem inconsistent with the largely fractured young surface of Europa [Pappalardo et al., 1999] and the interpretation of the surface features. The topography associated with these features would require thinner conductive lid (<5 km) [Nimmo and Manga, 2002]. Showman and Han [2003] have shown using 2-D numerical experiments that no significant uplifts are observed even with very small viscosity contrast (<10⁴), which are difficult to explain on the basis of ice creep experiments.

[59] This paradox may be due to an incorrect description of the internal dynamics of Europa's ice shell. The faulting and the localization of deformation in the conductive lid may (i) enhance tidal dissipation along faults, (ii) lead warm convective ice to be located at shallower depths, (iii) and allow partial melting closer to the surface. These effects could make the convective solutions very different, and far from the classical stagnant lid regime. Before proposing a consistent model for the “lenticulae” formation and the internal dynamics of the ice shell, numerical developments are required. We are currently incorporating damage rheology in our models in order to simulate the ice fatigue due to tidal deformation and the existence of faults, as well as to

investigate the effects of localized deformation within the conductive lid.

[60] In addition, the geometry of hot plumes and its surface manifestations can only be assessed in a 3D-geometry. Future developments in this direction are required. Finally, the possibility of downward melt percolation should be investigated and included in a more accurate model.

5. Conclusions

[61] From numerical experiments of thermal convection with strongly temperature-dependent viscosity and viscosity-dependent tidal heating, we show that tidal dissipation within Europa's convective ice layer is large enough to prevent the total freezing of the subsurface ocean. The ice layer is composed of a thick (35%–50% of the layer) conductive rigid shell overlying a convective sublayer, where most of the tidal dissipation occurs. Tidal heating can raise the temperature at the center of hot plumes up to the melting point. This induces episodic upwellings of partially molten ice up to the base of the conductive lid. Some similarities between the simulated convective instabilities and observed surface features (lenticulae and chaos regions), suggest that the rise of tidally heated ice could explain their formation. We are currently developing more detailed models including damage rheology within the lid in order to assess the link between the warm icy upwellings and the cold surface.

[62] Tidal heating strongly reduces the heat flux at the base of the ice layer, which becomes less efficient in transferring heat from the interior toward the surface. For Europa's present-day eccentricity, the globally averaged thickness of a convective ice shell in equilibrium with the silicate core is estimated to be about 20–25 km, mostly depending on the ice viscosity value near the melting point. Lateral variations of both tidal dissipation and temperature surface induce variations (~5 km) of the equilibrium thickness: maxima are obtained on both sides of the equator at the sub-Jovian and anti-Jovian points, and minima at mid-latitudes. The predicted tidal heating rate is four times larger at the poles than at the equator. However, the surface heat flux remains nearly constant over Europa's surface, due to a thinner dissipative convective sublayer at the poles than at the equator. The ice shell thickness variations should induce gravity field anomalies of the same order of magnitude than the one associated with time-varying tidal potential. These could be inferred from measurements of the gravitational potential by a future Europa orbiter mission, which would give a strong constraint on Europa's internal structure.

Appendix A: Corrected Thickness of the Conductive Lid

[63] The following equation describes the thermal evolution of a tidally heated conductive ice layer, with temperature-dependent thermal conductivity:

$$\frac{\partial T}{\partial t} = k(z) \frac{\partial^2 T(z)}{\partial z^2} + \frac{\partial k(z)}{\partial z} \frac{\partial T(z)}{\partial z} + H_{tide}(z), \quad (A1)$$

where $k(T) = 488.12/T(K) + 0.4685$, and H_{tide} is given by equation (13). A Crank-Nicholson method is used to solve

this equation. The layer is divided in n_s intervals of equal thickness dz . The surface temperature T_{surf} and the temperature at the base of the lid T_{lid} are prescribed. The initial profile is linear. After each timestep, the spatial interval dz is re-calculated in such a way that the bottom heat flux equals a prescribed value ϕ_{lid} . This procedure is iterated, until a steady-state solution is reached.

[64] The thickness of the conductive lid is calculated for different bottom and surface temperatures: $220 \geq T_{lid} \geq 240\text{K}$ and $60 \geq T_{surf} \geq 110\text{K}$, different bottom heat fluxes: $10 \geq \phi_{lid} \geq 100 \text{ mW.m}^{-2}$, and different values for H_{max} and η_{max} . In order to estimate how much the temperature dependence of thermal conductivity thickens the conductive lid, the thickening coefficient x_{lid} is defined as the ratio between the corrected thickness z_{lid}^c of the conductive lid (calculated here) and the thickness obtained for a constant thermal conductivity estimated at $T = 270\text{K}$:

$$x_{lid} = z_{lid}^c \times \left[\frac{k_{T=270\text{K}}(T_{lid} - T_{surf})}{\phi_{lid}} \right]^{-1} \quad (\text{A2})$$

Since the tidal heating in the conductive lid is relatively small, the values of H_{max} and η_{max} do not influence the thickness of the conductive lid. The coefficient x_{lid} mainly depends on surface temperature T_{surf} , and slightly depends on bottom temperature T_{lid} . For $T_{surf} = 60\text{K}$, $x_{lid} = 1.9-2$, depending on T_{lid} . For $T_{surf} = 100\text{K}$, $x_{lid} = 1.5-1.55$.

Appendix B: Calculation of the Total Ice Shell Thickness

[65] The corrected thickness of Europa's ice shell depends on both maximal tidal dissipation H_{max} and surface temperature T_{surf} . Since our numerical experiments are performed with dimensionless variables, the first stage of this calculation is to dimensionalize the effective ice shell thickness b , the surface and bottom heat fluxes, ϕ_{surf} and ϕ_{bot} , and the maximal tidal heating rate for H_{max} , for different values of the surface temperature T_{surf} (the bottom temperature being fixed to 270K). For each value of dimensionless parameters (Ra_{bot} , h_{max}), the four variables b , ϕ_{surf} , ϕ_{bot} and H_{max} are calculated as a function of $\Delta T = T_{bot} - T_{surf}$.

$$b = \left[\frac{Ra_{bot}\kappa\eta_{bot}}{\alpha g \Delta T} \right]^{-1/3} \quad (\text{B1})$$

$$\Rightarrow \phi_{bot} = \frac{k\Delta T}{b} \phi'_{bot}, \phi_{surf} = \frac{k\Delta T}{b} \phi'_{surf}, H_{max} = \frac{k\Delta T}{b^2} h'_{max}. \quad (\text{B2})$$

[66] For each value of the surface temperature, the surface and bottom heat fluxes are obtained for several H_{max} values (like in Figure 11) and for different Rayleigh number value, i.e., different effective thickness b values. From these values, linear relations between ϕ_{surf} and H_{max} , and ϕ_{bot} and H_{max} , are interpolated for each value of b and T_{surf} . Then, the value of H_{max} for which $\phi_{bot} = \phi_{sil}$ is determined. From the equilibrium values obtained with the numerical experiments, the equilibrium thickness b_{eq} as a function of H_{max} is extrapolated for different values of ϕ_{sil} and T_{surf} . A

map of the effective ice shell thickness in equilibrium with ϕ_{sil} is calculated from the map of maximal tidal dissipation H_{max} and from the map of surface temperature with this extrapolation.

[67] From our numerical experiments, we show that there is a relationship between the conductive lid thickness and the thickness of the whole layer:

$$z_{lid} = b \times [1.696 - 0.208 \times \log_{10}(Ra_{bot})]. \quad (\text{B3})$$

The effective thickness of the conductive lid is calculated from the Rayleigh number estimated for each value of b_{eq} and T_{surf} , with this formula, only valid for a viscosity ratio of 1.2×10^6 . Finally, the corrected thickness of the conductive lid is evaluated in function of the surface temperature from the thickening coefficient x_{lid} calculated following Appendix A, and the “real” thickness e_{ice} of the equilibrium ice shell is then derived.

[68] **Acknowledgments.** This work was supported by INSU-Programme National de Planétologie. We are grateful to Antoine Mocquet for his help with tidal dissipation calculations as well as Paul Duval for very helpful suggestions on ice rheology. We also thank Hauke Hussmann for discussions about the orbital and thermal evolution of Europa. Further thanks are extended to Gerald Schubert and an anonymous reviewer for their constructive comments.

References

- Anderson, J. D., G. Schubert, R. A. Jacobson, E. L. Lau, W. B. Moore, and W. L. Sjogren, Europa's differentiated internal structure: Inferences from four Galileo encounters, *Science*, **281**, 219–222, 1998.
- Biot, M. A., Theory of the stress-strain relations in anisotropic viscoelasticity and relaxation phenomena, *J. Appl. Phys.*, **25**, 1385–1391, 1954.
- Budd, W. F., and T. H. Jacka, A review of ice rheology for ice sheet modelling, *Cold Reg. Sci. Technol.*, **16**, 107–144, 1989.
- Carr, M. H., et al., Evidence for a subsurface ocean on Europa, *Nature*, **391**, 363–365, 1998.
- Cassen, P., R. T. Reynolds, and S. J. Peale, Is there liquid water on Europa?, *Geophys. Res. Lett.*, **6**, 731–734, 1979.
- Castillo, J., A. Mocquet, and C. Sotin, Détecter la présence d'un océan dans l'Europe à partir de mesures altimétriques et gravimétriques, *C. R. Acad. Sci. Ser. II*, **330**, 659–666, 2000.
- Christensen, U. R., Heat transport by variable viscosity convection and implications for the Earth's thermal evolution, *Phys. Earth Planet. Inter.*, **35**, 264–282, 1984.
- Cole, D. M., The microstructure of ice and its influence on mechanical properties, *Eng. Fract. Mech.*, **68**, 1797–1822, 2001.
- Collins, G. C., J. W. Head, R. T. Pappalardo, and N. A. Spaun, Evaluation of models for the formation of chaotic terrain on Europa, *J. Geophys. Res.*, **105**, 204–218, 2000.
- Dash, J. G., H. Fu, and J. S. Wetlaufer, The premelting of ice and its environmental consequences, *Rep. Progr. Phys.*, **58**, 115–167, 1995.
- Davaile, A., and C. Jaupart, Transient high-Rayleigh-number thermal convection with large viscosity variations, *J. Fluid Mech.*, **253**, 141–166, 1993.
- De La Chapelle, S., H. Milsch, O. Castelnau, and P. Duval, Compressive creep of ice containing a liquid intergranular phase: Rate-controlling processes in the dislocation creep regime, *Geophys. Res. Lett.*, **26**, 251–254, 1999.
- Deschamps, F., and C. Sotin, Thermal convection in the outer shell of large icy satellites, *J. Geophys. Res.*, **106**, 5107–5122, 2001.
- Dumoulin, C., M. Doin, and L. Fleitout, Heat transport in stagnant lid convection with temperature- and pressure-dependent Newtonian or non-Newtonian rheology, *J. Geophys. Res.*, **104**, 12,759–12,778, 1999.
- Durham, W. B., S. H. Kirby, and L. A. Stern, Creep of water ices at planetary conditions: A compilation, *J. Geophys. Res.*, **102**, 16,293–16,302, 1997.
- Durham, W. B., L. A. Stern, and S. H. Kirby, Rheology of ice I at low stress and elevated confining pressure, *J. Geophys. Res.*, **106**, 11,031–11,042, 2001.
- Duval, P., The role of the water content on the creep rate of polycrystalline ice, in *Isotopes and Impurities in Snow and Ice*, IAHS Publ., **118**, 29–33, 1977.

- Duval, P., and M. Montagnat, Comment on "Superplastic deformation of ice: Experimental observations" by D. L. Goldsby and D. L. Kohlstedt, *J. Geophys. Res.*, 107(B4), 2082, doi:10.1029/2001JB000946, 2002.
- Fagents, S. A., R. Greeley, R. J. Sullivan, R. T. Pappalardo, L. M. Prockter, and Galileo SSI Team, A cryomagnetic origin for low albedo features on Europa, *Lunar Planet. Sci.*, XXX, abstract 1296, 1999.
- Geissler, P. E., et al., Evolution of lineaments on Europa: Clues from Galileo multispectral imaging observations, *Icarus*, 135, 107–126, 1998.
- Goldsby, D. L., and D. L. Kohlstedt, Grain boundary sliding in fine-grained ice I, *Ser. Mater.*, 37, 1399–1406, 1997.
- Goldsby, D. L., and D. L. Kohlstedt, Superplastic deformation of ice: Experimental observations, *J. Geophys. Res.*, 106, 11,017–11,030, 2001.
- Grasset, O., and E. M. Parmentier, Thermal convection in a volumetrically heated, infinite Prandtl number fluid with strongly temperature-dependent viscosity: Implications for planetary evolution, *J. Geophys. Res.*, 103, 18,171–18,181, 1998.
- Grasset, O., and C. Sotin, The cooling rate of a liquid shell in Titan's interior, *Icarus*, 123, 101–112, 1996.
- Grasset, O., C. Sotin, and F. Deschamps, On the internal structure and dynamics of Titan, *Planet. Space Sci.*, 48, 617–636, 2000.
- Greenberg, R., P. Geissler, G. Hoppa, B. R. Tufts, D. D. Durda, R. Pappalardo, J. W. Head, R. Greeley, R. Sullivan, and M. H. Carr, Tectonic processes on Europa: Tidal stresses, mechanical response, and visible features, *Icarus*, 135, 64–78, 1998.
- Greenberg, R., G. V. Hoppa, B. R. Tufts, P. Geissler, J. Riley, and S. Kadel, Chaos on Europa, *Icarus*, 141, 263–286, 1999.
- Hobbs, P. V., *Ice Physics*, Clarendon, Oxford, England, 1974.
- Hussmann, H., and T. Spohn, Coupled thermal-orbital evolution of Europa, *Eos Trans. AGU*, 83(47), Fall Meet. Suppl., abstract P72B-0505, 2002.
- Hussmann, H., T. Spohn, and K. Wieczerkowski, Thermal equilibrium states of Europa's ice shell: Implications for internal ocean thickness and surface heat flow, *Icarus*, 156, 143–151, 2002.
- Khurana, K. K., M. G. Kivelson, D. J. Stevenson, G. Schubert, C. T. Russel, R. J. Walker, and C. Polanskey, Induced magnetic fields as evidence for subsurface oceans in Europa and Callisto, *Nature*, 395, 777–780, 1998.
- McKinnon, W. B., Convective instability in Europa's floating ice shell, *Geophys. Res. Lett.*, 26, 951–954, 1999.
- Montagnat, M., and P. Duval, Rate controlling processes in the creep of polar ice, influence of grain boundary migration associated with recrystallization, *Earth Planet. Sci. Lett.*, 183, 179–186, 2000.
- Moore, W. B., and G. Schubert, NOTE: The tidal response of Europa, *Icarus*, 147, 317–319, 2000.
- Moresi, L. N., and V. S. Solomatov, Numerical investigation of 2D convection with extremely large viscosity variations, *Phys. Fluids*, 7, 2154–2162, 1995.
- Nimmo, F., and M. Manga, Causes, characteristics and consequences of convective diapirism on Europa, *Geophys. Res. Lett.*, 29(23), 2109, doi:10.1029/2002GL015754, 2002.
- Nye, J. F., Thermal behaviour of glacier and laboratory ice, *J. Glaciol.*, 35, 17–22, 1989.
- Nye, J. F., and S. Mae, The effect of non-hydrostatic stress on intergranular water veins and lenses in ice, *J. Glaciol.*, 11, 81–101, 1972.
- Ojakangas, G. W., and D. J. Stevenson, Thermal state of an ice shell on Europa, *Icarus*, 81, 220–241, 1989.
- Pappalardo, R. T., et al., Geological evidence for solid-state convection in Europa's ice shell, *Nature*, 391, 365–368, 1998.
- Pappalardo, R. T., et al., Does Europa have a subsurface ocean? Evaluation of the geological evidence, *J. Geophys. Res.*, 104, 24,015–24,056, 1999.
- Parmentier, E. M., C. Sotin, and B. J. Travis, Turbulent 3-D thermal convection in an infinite Prandtl number, volumetrically heated fluid: Implications for mantle dynamics, *Geophys. J. Int.*, 116, 241–251, 1994.
- Reese, C. C., V. S. Solomatov, and L.-N. Moresi, Non-Newtonian stagnant lid convection and magmatic resurfacing on Venus, *Icarus*, 139, 67–80, 1999.
- Ruiz, J., The stability against freezing of an internal liquid-water ocean in Callisto, *Nature*, 412, 409–411, 2001.
- Schubert, G., D. L. Turcotte, and P. Olson, Internal heat sources and time dependence, in *Mantle Convection in the Earth and Planets*, pp. 382–385, Cambridge Univ. Press, New York, 2001a.
- Schubert, G., D. L. Turcotte, and P. Olson, Numerical models of three-dimensional convection, in *Mantle Convection in the Earth and Planets*, pp. 417–498, Cambridge Univ. Press, New York, 2001b.
- Segatz, M., T. Spohn, M. N. Ross, and G. Schubert, Tidal dissipation, surface heat flow, and figure of viscoelastic models of Io, *Icarus*, 75, 187–206, 1988.
- Showman, A. P., and L. Han, Numerical simulations of convection in Europa's ice shell: Implications for surface features, *Lunar Planet. Sci.*, XXXIII, abstract 1806, 2003.
- Smolarkiewicz, P. K., A fully multidimensional positive definite advection transport algorithm with small implicit diffusion, *J. Comput. Phys.*, 54, 325–362, 1984.
- Sohl, F., T. Spohn, D. Breuer, and K. Nagel, Implications from Galileo observations on the interior structure and chemistry of the Galilean satellites, *Icarus*, 157, 104–119, 2002.
- Solomatov, V. S., Scaling of temperature- and stress-dependent viscosity convection, *Phys. Fluids*, 7, 266–274, 1995.
- Sotin, C., J. W. Head III, and G. Tobie, Europa: Tidal heating of upwelling thermal plumes and the origin of lenticulae and chaos melting, *Geophys. Res. Lett.*, 29(8), 1233, doi:10.1029/2001GL013844, 2002.
- Spohn, T., and G. Schubert, Oceans in the icy Galilean satellites of Jupiter, *Icarus*, 161, 456–467, 2003.
- Squyres, S. W., R. T. Reynolds, and P. M. Cassen, Liquid water and active resurfacing on Europa, *Nature*, 301, 225–226, 1983.
- Stevenson, D. J., Limits on the variation of thickness of Europa's ice shell, *Lunar Planet. Sci.*, XXXI, abstract 1506, 2000.
- Takeuchi, H., and M. Saito, Seismic surface waves, in *Methods in Computational Physics*, vol. 11, edited by B. Alder et al., pp. 217–295, Academic, San Diego, Calif., 1972.
- Thomson, R. E., and J. R. Delaney, Evidence for a weakly stratified European ocean sustained by seafloor heat flux, *J. Geophys. Res.*, 106, 12,355–12,366, 2001.
- Tobie, G., G. Choblet, A. Mocquet, J. Pargamin, and C. Sotin, Tidally heated convection within Europa's ice shell, *Lunar Planet. Sci.*, XXXIII, abstract 1498, 2002.
- Travis, B., P. Olson, and G. Schubert, The transition from two-dimensional to three-dimensional planforms infinite-Prandtl-number thermal convection, *J. Fluid. Mech.*, 216, 71–91, 1990.
- Vaughn, D. G., Tidal flexure at ice shelf margins, *J. Geophys. Res.*, 100, 6213–6224, 1995.
- Wang, H., and D. J. Stevenson, Convection and internal melting of Europa's ice shell, *Lunar Planet. Sci.*, XXXI, abstract 1293, 2000.
- Zschau, J., Tidal friction in the solid Earth: Loading tides versus body tides, in *Tidal Friction and the Earth's Rotation*, pp. 62–94, Springer-Verlag, New York, 1978.

G. Choblet, C. Sotin, and G. Tobie, Laboratoire Planétologie and Géodynamique, Université de Nantes, 2, rue de la Houssinière, 44321 Paris cedex 03, Nantes, France. (tobie@chimie.univ-nantes.fr)